



OPEN Investigation of vanadium oxide/activated carbon composites

Monika Dumka¹, Sakshi Juyal¹, Akansha Rajput¹, Fateh Singh Gill¹✉, Ankit Sharma², Ajay Kumar³, Vijay Kumar⁴ & Perumal Asaithambi⁵✉

Vanadium, known for its low cost, multiple valencies, and exceptional theoretical capacitance (pseudo-capacitance), has been investigated for energy applications. Activated carbon (AC) with its conductive and absorptive properties (EDLC behavior), is a well-established material. The composites synthesized from vanadium and derived ACs from various biomass sources have been reported in the literature. This paper also reports the synthesis of VO₂ nanomorphology on coconut shell-derived activated carbon using a hydrothermal method. SEM and TEM images indicated the VO₂ nanorods grown around AC micro-sized particles and fully interacting with each other. A sample containing more activated charcoal exhibited 545.56 F g⁻¹ specific capacity at 0.6 A g⁻¹ current density, which is 8% higher than the sample with less activated charcoal, and it also demonstrated negligible charge transfer resistance. The calculated b value confirmed the mechanism of charge storage. Vanadium has also insulin-enhancing properties for humans; therefore, the synthesized composites were also tested for anti-microbial activity. The results showed that it demonstrated bactericidal activity by inhibiting respiration and damaging the cellular components.

Keywords Vanadium oxide nanorods, Activated carbon, Electrochemical, Electrochemical-impedance-spectroscopy, Anti-microbial

Transition metal oxides (TMOs) are a class of material possessing a wide range of unusual electric, magnetic, and optical properties as a result of a partially filled outermost d-shell. Current progress in the field of nanostructuring has promoted the development of TMO nanostructures with enhanced surface area that exhibit modified physical and chemical properties as compared to TMOs. For example, nanostructuring TiO₂ increases the surface area-to-volume ratio exposing more active sites for catalytic reactions¹, VO₂ undergoes a well-known metal-insulator transition on size reduction², ZnO nanorods exhibit enhanced ultraviolet emission due to quantum confinement effects making them suitable for use in optoelectronic devices³, Fe₃O₄ nanoparticles exhibit superparamagnetism at room temperature⁴. Existing in multiple oxidation states and the ability of TMOs to undergo reversible redox and intercalation reactions make them suitable for energy storage applications⁵.

Some TMOs exhibiting photocatalytic properties (like ZnO, TiO₂) also generate Reactive Oxygen Species (ROS) such as superoxide anion(O₂⁻), hydrogen peroxide(H₂O₂), hydroxyl radical(·OH), and single oxygen (·O) that can cause oxidative stress in bacterial cells. This cellular damage can lead to cell membrane disruption, enzyme inactivation, and ultimately, bacterial cell death. In addition, some TMOs like CuO, ZnO, and Ag₂O, can release metal ions (e.g., Cu²⁺, Zn²⁺, Ag⁺) into the bacterial cell membranes, hence leading to cellular contents leakage, and resulting in cell death. These combinations of properties make TMO effective antimicrobial agents, with potential applications in healthcare, food preservation, and environmental protection⁶. Nanostructures of TMOs possess enhanced antibacterial properties due to increased surface area, enhanced generation of reactive oxygen species (ROS), and improved interaction with bacterial cell membranes, hence making them efficient anti-microbial agents.

Among TMOs, vanadium oxide (VO) is established for its promising electrochemical properties in energy storage applications. However, challenges such as its low conductivity and structural stability are issues. As mentioned above, TMOs such as TiO₂, ZnO, and CuO have antimicrobial properties. Nanostructuring further amplifies these effects, improving bacterial interaction and oxidative stress induction. Despite these advantages, the investigation of the antibacterial potential of VO-based compounds is needed.

¹Department of Allied Sciences, Graphic Era Deemed to be University, Bell Road, Clement Town, Dehradun, Uttarakhand 248002, India. ²Chitkara University Institute of Engineering and Technology, Chitkara University, Punjab 140401, India. ³Department of Mechanical Engineering, Noida Institute of Engineering and Technology, Delhi, India. ⁴Department of Mechanical Engineering, Thapar Institute of Engineering and Technology, Patiala, India. ⁵Faculty of Civil and Environmental Engineering, Jimma Institute of Technology, Jimma University, Po Box - 378, Jimma, Ethiopia. ✉email: ; asaithambi.perumal@ju.edu.et; drasaithambi2014@gmail.com

This work reports the charge storage properties along with antibacterial properties of vanadium oxide (VO) and purchased coconut-shell derived activated carbon (AC)-based composite prepared via the hydrothermal technique. The nanocomposite samples were prepared by varying weight percent ratios of vanadium and AC. Further, these were characterized through SEM, TEM, and RAMAN. Their electrochemical properties were studied using CV (cyclic voltammetry), GCD (Galvanostatic charge–discharge), and EIS (Electrochemical impedance spectroscopy) in 3-electrode configurations. Additionally, the composites' antimicrobial activity was evaluated by a well-diffusion method against gram-negative and gram-positive bacteria.

Experimental

Material and synthesis of nanocomposite samples

AC was purchased from Merck (up to 50 μm sized particles), and bulk VO_2 (99% purity) was purchased from SRL Pvt. Ltd., India. The composite of vanadium oxide and activated carbon was prepared through a one-step hydrothermal process at 160 $^\circ\text{C}$ for 5 h.

AC and bulk VO_2 were taken in weight ratios 1:3 and 3:1, and the resulting composites were named VO1/AC3 and VO3/AC1, respectively. The mixture (3 g AC with 1 g VO_2) was mixed in DI water, and 5 ml H_2O_2 (30% concentration, CDH, India) was added to the solution. A reddish to reddish-brown color change was observed after stirring and sonicating for 1 Hr each. Later, the composition of AC and bulk VO_2 was changed to 1 g and 3 g, respectively. After uniform dispersion of the solution, the contents were poured into a hydrothermal autoclave (100 ml) and treated at 160 $^\circ\text{C}$ for 5 h. After the autoclave cooled down, the contents of the autoclave were washed using DI water and ethanol alternately till a neutral pH was achieved. The product thus obtained was then dried in a muffle furnace at 150 $^\circ\text{C}$ for 2 h and then collected for testing and charge-storage evaluation.

Morphological and electrochemical evaluation

Scanning Electron Microscopy (SEM, Model: Zeiss Gemini 300) was done to observe the morphology of the composite, and Transmission Electron Microscopy (TEM, Model: TALOS F200X) analysis was done to study the internal structure of the material. RAMAN spectroscopy was done to analyze a sample's chemical composition and structure and find the degree of graphitization obtained. Electrochemical Analysis was done to study the charge storage properties of the material through Cyclic Voltammetry (CV), Galvanostatic charge–discharge (GCD), and Electrochemical Impedance Spectroscopy (EIS).

Antibacterial study

The vanadium oxide NPs' antibacterial activity against *Escherichia coli* (gram-negative (-)) and *Staphylococcus aureus* (gram-positive (+)) bacterial strains was determined using a well diffusion method. A cleaned and autoclaved petri dish was filled with nutrient agar medium and allowed to solidify. After solidification 5 circular wells (5 mm) were created using a borer and 4 wells filled with different nanoparticles dispersed in distilled water at different concentrations (25, 50, 75, and 100 μL). One well filled with antibiotic ampicillin (1 mg/ml) was taken as a control. Afterward, 1 mL of bacteria culture (O.D. = 1 at 600 nm) was spread onto the medium using a spreader and incubated at 37 $^\circ\text{C}$. After 24 h zone of inhibition of bacteria was measured to the antimicrobial activity of the prepared nanomaterial.

Results and discussion

Morphology

The SEM images of VO3/AC1 and VO1/AC3 are displayed in Fig. 1a,b, showing the presence of VO_2 nanorods (VONRs) enwrapped around activated carbon.

Due to the excess amount of VO_2 in VO3/AC1, VONRs are formed in abundance, and AC can be seen enwrapped with the NRs in Fig. 1a. Small NRs of VO_2 are visible in Fig. 1b inside the AC's porous matrix where AC is in excess amount than VO_2 . The formation of NRs can be attributed to the self-assembly of nanocrystals, where the growth of nuclei into nanorods is anisotropic, i.e., growth rates vary along different crystallographic directions. In the case of V_2O_5 , the layered structure of the material promotes faster growth along the c axes, leading to the formation of rod-like structures⁷. Figure 1c,d show TEM images of VO3/AC1 and VO1/AC3, respectively, where the formation of VO_2 NRs enwrapped around AC is evident.

Raman analysis

RAMAN bands of the material in Fig. 2 show the three prominent bands at 181, 1341, and 1592 cm^{-1} . The low wavenumber band around 180 cm^{-1} is attributed to V–O–V bending/wagging and V–O–V stretching modes present in VO_2 , which is characterized by a layered structure⁸. In addition, the D and G bands located at 1341 and 1592 cm^{-1} are associated with carbon atoms in various hybridization modes, and higher intensity peaks for sample VO1/AC3 are due to the abundance of carbon. The integrated area ratios of D and G bands (I_D/I_G) are approximately 2.34 and 2.21 for VO1/AC3 and VO3/AC1, respectively⁹. The low value of $I_D/I_G = 2.21$ in the composite with higher AC content (VO3/AC1) indicates improved graphitization and fewer defects compared to the sample with less AC (VO1/AC3). Increased graphitization also leads to improvement in the conductivity of the composite¹⁰, which is also indicated by the low equivalent series resistance value of VO3/AC1 in EIS analysis.

Antibacterial study

To study the effect of inhibition under *S. aureus* and *E. coli* bacterial culture after 24 h of incubation, vanadium and a sample containing more AC were selected for comparison (See Fig. 3).

The activity of NPs and the control was performed against the specified bacterial strain. The inhibition zones' diameters are presented in Table 1. The vanadium oxide NPs showed inhibition zones of 20 mm, 25 mm,

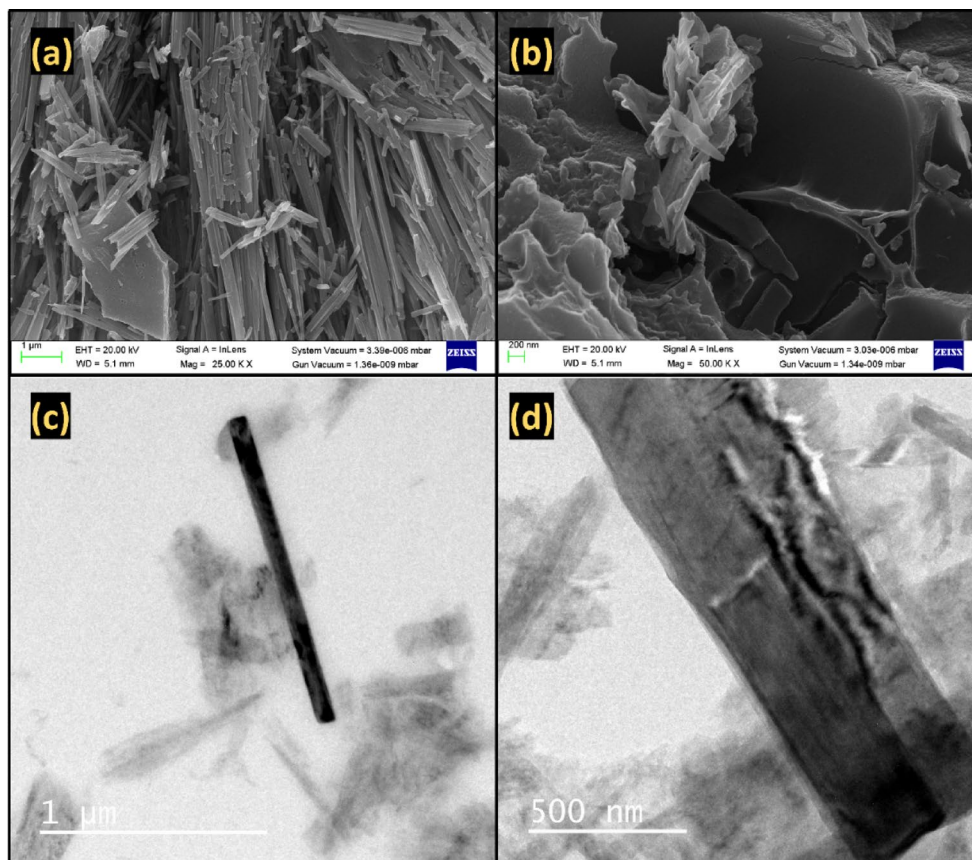


Fig. 1. SEM image (a) and (b) VONRs in sample VO3/AC1, (c) and (d) a VONR wrapped with AC in sample VO3/AC1 and VO1/AC3, respectively.

18 mm, and 30 mm in *S. aureus* and 15 mm, 14 mm, 20 mm, and 10 mm in *S. aureus* at 25, 50, 75, and 100 mg/mL concentrations, respectively^{10,11}. Similarly, the inhibition zone produced by VO1/AC3 NPs were 10 mm, 15 mm, 20 mm, and 20 mm in *S. aureus* and 10 mm, 10 mm, 16 mm, and 25 mm at 25, 50, 75, and 100 mg/mL, respectively.

These results indicate that both vanadium oxide NPs and VO1/AC3 NPs exhibited antimicrobial effectiveness against *S. aureus* in a concentration-dependent manner, with larger inhibition zones observed at higher concentrations. Vanadium oxide NPs demonstrated superior antibacterial activity compared to VO1/AC3 NPs, as indicated by consistently larger inhibition zones. These findings highlight the potential for vanadium oxide-based nanomaterials in antimicrobial applications, which require further investigation to improve their mechanisms of action and effectiveness.

Electrochemical analysis

The materials were tested as active materials for supercapacitor electrodes by coating their slurry on a conducting substrate and using it as a working electrode. The charge storage properties were measured using a 3-electrode cell with the material VO3/AC1 and VO1/AC3 as a working electrode. Platinum wire and Ag/AgCl served as the counter electrode, and reference electrode respectively, in a 1 Mole Na₂SO₄ electrolyte. The CV, GCD, and EIS were used to evaluate the nature of charge storage, specific capacitance, and impedance behavior of the active material.

The redox peaks in CV curves, along with slant shapes in Fig. 4a,b, show a mixed mechanism of charge storage. This shows that the total capacitive current from both VO1/AC3 and VO3/AC1 is the result of EDLC current from AC and pseudocapacitive current from VO₂ NRs. It can also be observed that the redox peaks in the CV of VO1/AC3 and VO3/AC1 are more prominent at lower scan rates due to the formation of a steady state between the electrochemical reaction and reactants. Also, the area enclosed by the CV loop is indicative of the charge stored by the material, which is larger for VO3/AC1 than VO1/AC3 at the same 100 mVs⁻¹ scan rate, showing better charge storage¹².

Further investigation of CV curves was done to calculate the b value, which is mathematically equal to the slope of the log(scan rate) versus log(current density) curve, as shown in Fig. 4c,d. Figure 4d represents the b values for VO1/AC3 and VO3/AC1 as 0.69 and 0.94, respectively. b value helps determine whether the charge storage is primarily governed by surface redox reactions (capacitive behavior) or diffusion-controlled processes (Faradaic behavior). b = 0.5 indicates a diffusion-controlled process, typically associated with faradaic reactions (like battery-type behavior where ion diffusion limits the rate of charge storage), and b = 1.0 indicates a capacitive

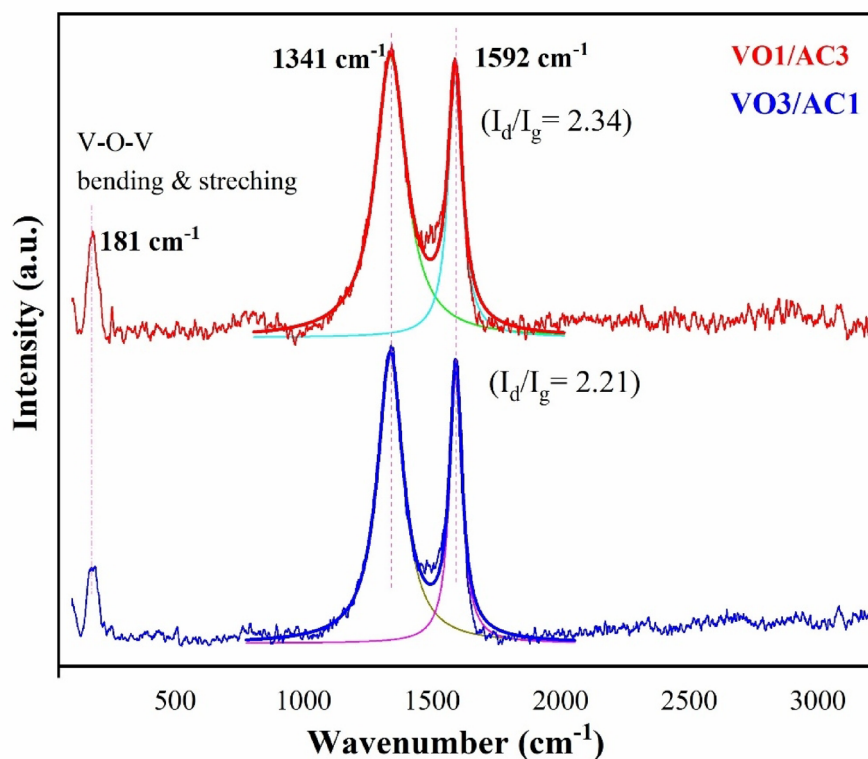


Fig. 2. RAMAN spectra of VO₁/AC₃ and VO₃/AC₁ samples.

process, meaning the charge is stored primarily via surface reactions (pseudocapacitance). Hence, $b = 0.64$ for VO₁/AC₃ is a marker of diffusion-limited charge storage, often associated with slower Faradaic processes in contrast to $b = 0.94$ for VO₃/AC₁, for which charge storage is capacitive dominated¹³.

Conclusively, VO₁/AC₃ ($b = 0.69$) demonstrates diffusion-limited charge storage, which is related to slow Faradaic processes, while VO₃/AC₁ ($b = 0.94$) demonstrates capacity-dominated charge storage, which allows for rapid charge–discharge cycles.

A galvanostatic charge–discharge test was performed to calculate and compare the discharge times of the electrodes, and specific capacitance was calculated using the Eq. (1). Further energy density and power density were also calculated through Eqs. (2) and (3), which are summarised in Table 2. The shape of the GCD curves has a plateau-like feature instead of straight lines. The non-linear shape points towards the Faradaic behavior of charge storage in the electrode, which is also evident from the presence of peaks in CV curves of the electrodes. Figure 5a,b show the voltage variation response of composites with increasing time at constant currents 2, 5, 7, 10, and 12 mA. The VO₁/AC₃ composite shows specific capacitance of 545.56, 266.29, 166.80, 132.40, and 118.55 while VO₃/AC₁ shows specific capacitance of 503.25, 256.77, 194.39, 139.87, and 117.57 at 2, 5, 7, 10, and 12 mA current, respectively depicted in Fig. 5c. Figure 5c also shows that the VO₁/AC₃ composite shows better capacitance and capacitive retention as compared to VO₃/AC₁, reflecting that AC is responsible for providing better charge storage and better synergy between components, vanadium oxide and carbon at a 1:3 weight ratio. However, the potential drop (IR drop), which is caused by an additional resistance, the uncompensated resistance, experienced by VO₁/AC₃ is larger as compared to VO₃/AC₁, showing that the internal resistance is larger in VO₁/AC₃ as seen in Fig. 5d. This assumption is supported by the results of the EIS analysis, which is discussed later.

The values of discharge time were used for calculating specific capacitance (C) using the following equation¹⁴:

$$C = (I \cdot \Delta t) / (m \cdot \Delta V) \quad (1)$$

where ' I ' is the current, ' m ' is the active mass loading, which is taken as 1 mg, Δt is the discharge time, and ΔV is the voltage window.

Also, energy density and power density were calculated through the following equations¹⁴:

$$E = (1/2) \cdot C \cdot \Delta V^2 \quad (2)$$

$$P = E/\Delta t \quad (3)$$

The values of ' C ', ' E ' and ' P ' are tabulated in Table 2.

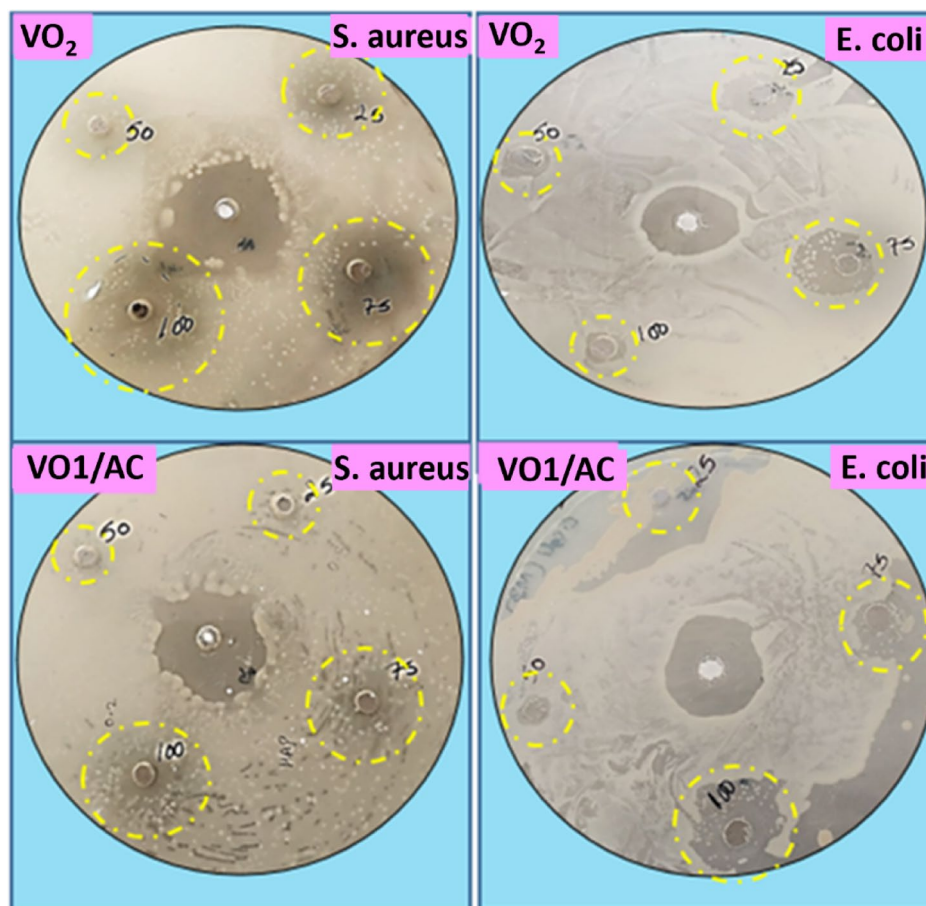


Fig. 3. Diameter of inhibition under *E. coli* and *S. aureus* bacterial culture (24 h of incubation).

Diameter of inhibition (mm)				
Concentration (μL)	VO ₂ nanorods		VO1/AC3	
	<i>S. aureus</i>	<i>E. coli</i>	<i>S. aureus</i>	<i>E. coli</i>
25	25	15	14	10
50	20	14	15	10
75	18	20	20	16
100	30	10	20	25

Table 1. Diameter of inhibition for different microorganisms.

EIS testing was done to calculate the prepared electrodes' equivalent series resistance R_s , charge-transfer resistance, and ion diffusion. The Nyquist plots of VO3/AC1 and VO1/AC3 electrodes are displayed in Fig. 6. The intercept of the curves on the x-axis gives the series resistance (R_s) of the electrodes, whereas in the high-frequency region, the semicircle diameter indicates the charge transfer resistance. The value of R_s for VO3/AC1 and VO1/AC3 was found to be 12.8 and 17.5, respectively and showed that the solution resistance increases.

when the ratio of AC increased in the composite. As the ratio increases in the composite, the absence of a semi-circle in the high-frequency region shows indicates low charge transfer resistance and promote facile ion diffusion in the electrode material¹⁵. The result collaborates well with the values of potential drop obtained from the GCD curves.

The electrochemical results show that the higher ratio of the composite sample (VO3/AC1) offers less resistance as compared to the sample containing low vanadium oxide (VO1/AC3) of the composite; however, a higher ratio of AC is responsible for higher charge storage properties. Furthermore, the electrochemical parameters of vanadium and other metal oxide composites have been presented in Table 3.

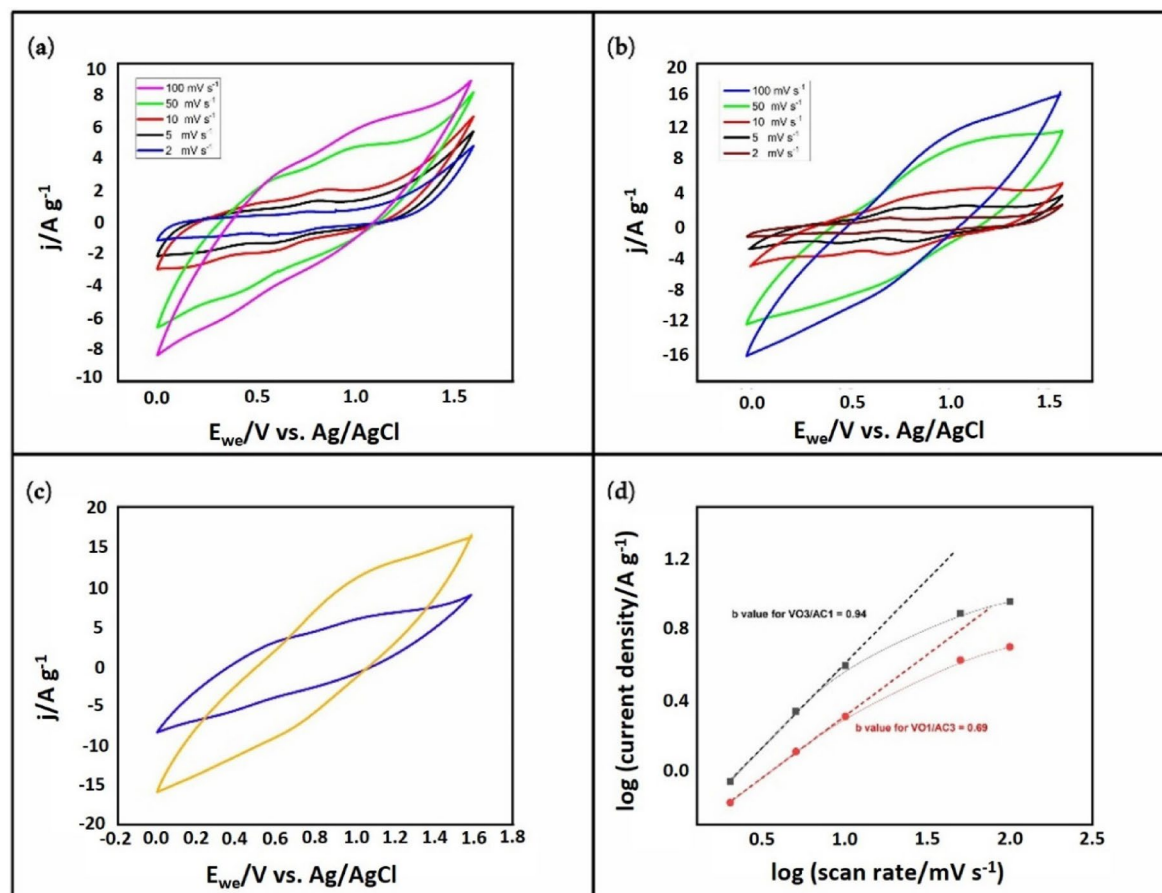


Fig. 4. (a) VO1/AC3, (b) VO3/AC1, (c) comparison of CVs at 100 mV s⁻¹, (d) Calculated 'b' value of VO1/AC3 and VO3/AC1.

Current density (A g ⁻¹)	Discharge time (s)	Potential drop (mV)	Specific capacitance (C) (F g ⁻¹)	Energy density (E) (Wh kg ⁻¹)	Power density (P) (W kg ⁻¹)
VO1/AC3					
1	862	65	545.56	189.16	790
2.5	168.3	149	266.29	92.33	1975
3.5	75.3	217	166.80	57.83	2765
5	41.84	312	132.40	45.90	3950
6	31.22	374	118.55	41.10	4740
VO3/AC1					
0.6	1207.8	50	503.25	178.93	533.33
1.6	246.5	103	256.77	91.29	1333.33
2.3	133.3	157	194.39	69.11	1866.66
3.3	67.14	288	139.87	49.73	2666.66
4	47.03	344	117.57	41.80	3200

Table 2. Electrochemical parameters in three cell study.

Conclusion

The composites synthesized by varying concentrations of VO₂ and AC through hydrothermal were studied. Their anti-microbial and charge storage properties were investigated. SEM, TEM, and RAMAN spectroscopy confirmed the formation of vanadium oxide nanorods with AC. The higher AC content sample (VO₃/AC1) exhibited better capacitance, energy density, and power density than the sample with less AC (VO₁/AC3). The AC was found to contribute to a synergistic effect to the composite. Whereas, the calculated 'b' value of (VO₃/AC1) exhibited capacitive-dominated charge storage, and the sample AC (VO₁/AC3) exhibited diffusion-limited charge storage. The antimicrobial properties of pure vanadium oxide were found to be better than those of its composite with AC.

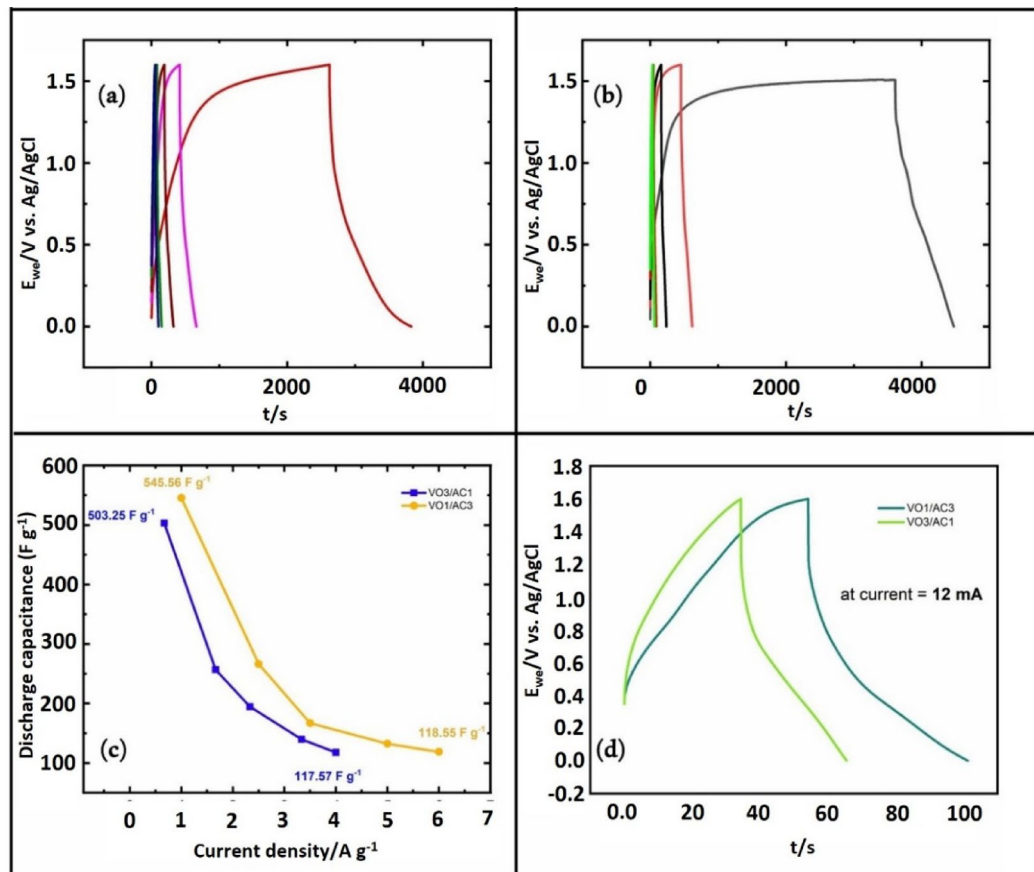


Fig. 5. GCD curves for (a) VO3/AC1, (b) VO1/AC3, (c) variation of specific capacitance with various current density (2, 5, 7, 10, and 12 mA) for composite VO1/AC3 and VO3/AC1, (d) comparison of discharge time and potential drop for composite VO1/AC3 and VO3/AC1 at current 12 mA.

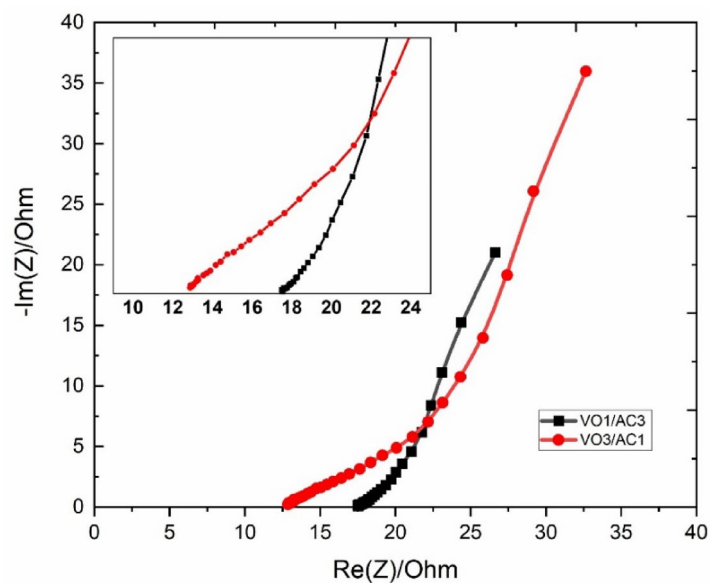


Fig. 6. Nyquist plot of VO1/AC3 and VO3/AC1.

Composite	Method used	Electrolyte	Specific capacitance	References
VO ₂ (B) nanobelts/rGO	Hydrothermally grown VO ₂ on rGO	0.5 M K ₂ SO ₄	353 F g ⁻¹ @1 A g ⁻¹	16
V ₂ O ₃ /N-rGO nanoflakes	NH ₃ reduction of V ₂ O ₅ gel/GO films	1 M Na ₂ SO ₄	216 mF cm ⁻²	17
V ₂ O ₃ nanocomposites	Calcination of hydrothermally grown (NH ₄) ₂ V ₃ O ₈	5 M LiCl	458.6 F g ⁻¹	18
V ₂ O ₃ @C core-shell nanorods	Single pot hydrothermal process using V ₂ O ₅ nanorod	5 M LiCl	228 F g ⁻¹	19
V ₂ O ₃ nanofoam@activated carbon	Calcination of NH ₄ VO ₃ solution and activated C	NaNO ₃	185 F g ⁻¹	20
rGO/V ₂ O ₅ nanosheet	Mixing rGO with hydrothermally grown V ₂ O ₅	1 M KCl	653 F g ⁻¹ @1 A g ⁻¹	21
rGO/V ₂ O ₅ hybrid aerogel	One-pot Hydrothermally grown	1 M LiClO ₄ / PPC	384 F g ⁻¹ @1 A g ⁻¹	22
NVO-PAC (Ammonium vanadium oxide and porous activated carbon)	-	NH ₄ SO ₄	367 mF cm ⁻² @2 mA cm ⁻²	23
Vanadium oxide composite electrodes	Vanadium oxide composite electrodes with an embedded conducting network of CNTs	-	350 mA h g ⁻¹	24
Bamboo-based activated carbon @ MnO ₂ nanocomposites	Bamboo-based AC powder and KMnO ₄ were dispersed in DI water, followed by hydrothermal synthesis	1 M Na ₂ SO ₄	221.45 F g ⁻¹	25
Birnessite-type MnO ₂ /AC nanocomposite	Chemical precipitation of MnO ₂ from KMnO ₄ in a solution containing AC	1 M Na ₂ SO ₄	210 F g ⁻¹	26
Activated mesocarbon microbead/Mn ₂ O ₄ composite	Physical adsorption of Mn(NO ₃) ₂ on the surface of activated microbeads, followed by annealing	1 M LiPF ₆ / (EC + DMC)	178 F g ⁻¹	27
Activated carbon loaded with nickel oxide	Suspending AC in Ni(NO ₃) ₂ solution, followed by neutralization	6 M KOH	194.01 F g ⁻¹	28
λ-MnO ₂ /carbon	Treating LiMn ₂ O ₄ /carbon powder with diluted sulphuric acid	1 M Na ₂ SO ₄	120 F g ⁻¹	29
MnO ₂ /AC	Bio-char derived AC and KMnO ₄ were dispersed together in DI water, followed by stirring and drying	1 M KOH	1126 F g ⁻¹	30
Activated coconut-shell carbon and hydrous ruthenium oxide (RuO _x (OH))	Sonication of AC in a colloidal solution of RuO _x (OH)	1 M H ₂ SO ₄	250 F g ⁻¹	31
RuO _x /carbon composite	RuCl ₃ colloidal particles absorbed on Carbon black powder, followed by annealing	1 M H ₂ SO ₄	863 F g ⁻¹	32
Hydrous ruthenium oxide/mesoporous carbon composite	Impregnating ruthenium(III) acetylacetonate into a mesoporous carbon followed by annealing through chemical vapor impregnation method	2.0 M H ₂ SO ₄	243 F g ⁻¹	33
RuO ₂ -C composite	Electroless deposition of Ru on activated carbon in an alkaline bath	1 M H ₂ SO ₄	265 F g ⁻¹	34
(ZnO)-AC composite electrode	ZnO-AC electrode is prepared at room temperature by a co-precipitation method	0.1 M Na ₂ SO ₄	106.1 mF cm ⁻²	35

Table 3. Electrochemical parameters of vanadium and other metal oxide composites.

Data availability

The data supporting the findings of this study are available on request from Mrs. Monika Dumka.

Received: 5 May 2025; Accepted: 26 June 2025

Published online: 25 September 2025

References

- Dey, S. & Mehta, N. S. Synthesis and applications of titanium oxide catalysts for lower temperature CO oxidation. *Curr. Res. Green Sustain. Chem.* **3**, 100022 (2020).
- Hongwei, L. et al. Size effects on metal-insulator phase transition in individual vanadium dioxide nanowires. *Opt. Express* **22**(25), 30748–30755 (2014).
- Norek, M. Approaches to enhance UV light emission in ZnO nanomaterials. *Curr. Appl. Phys.* **19**(8), 867–883 (2019).
- Caruntu, D., Caruntu, G. & O'Connor, C. J. Magnetic properties of variable-sized Fe₃O₄ nanoparticles synthesized from non-aqueous homogeneous solutions of polyols. *J. Phys. D Appl. Phys.* **40**(19), 5801 (2007).
- Liang, R. et al. Transition metal oxide electrode materials for supercapacitors: a review of recent developments. *Nanomaterials* **11**(5), 1248 (2021).
- Pandey, P. P. Nano-biomaterials in antimicrobial therapy. In *Recent Advances in Biopolymers* (IntechOpen, 2016).
- Ramasamy, K. & Gupta, A. Routes to self-assembly of nanorods. *J. Mater. Res.* **28**(13), 1761–1776 (2013).
- Shaohong, Z., Juan, F., Qiucheng, S., Liangpeng, W. & Xinjun, L. In situ characterization on thermal transitions of VO₂ (B): Toward VO₂ (R) and V₂O₃. *Rare Metal Mater. Eng.* **45**(6), 1374–1380 (2016).
- Jeidi, H. et al. Production and characterization of carbon-vanadium nanocomposites. *J. Mater. Sci.: Mater. Electron.* **33**(29), 22957–22970 (2022).
- Sekar, S. et al. Graphitic carbon-encapsulated V₂O₅ nanocomposites as a superb photocatalyst for crystal violet degradation. *Environ. Res.* **205**, 112201 (2022).
- Prasad, K. S. & Ramachandrapa, S. U. Potential medicinal applications of vanadium and its coordination compounds in current research prospects: A review. *Curr. Bioact. Compd.* **16**(3), 201–209 (2020).
- Zhang, L. & Gong, H. Improvement in flexibility and volumetric performance for supercapacitor application and the effect of Ni-Fe ratio on electrode behaviour. *J. Mater. Chem. A* **3**(14), 7607–7615 (2015).
- Kumar, K. S. et al. Investigating 2D WS₂ supercapacitor electrode performance by Kelvin probe force microscopy. *J. Mater. Chem. A* **8**(25), 12699–12704 (2020).
- Sharma, S. & Chand, P. Supercapacitor and electrochemical techniques: A brief review. *Results Chem.* **5**, 100885 (2023).
- Zhang, J., Wang, S. & Ono, K. Electrochemical impedance spectroscopy. In *Microscopy and Microanalysis for Lithium-Ion Batteries* 301–350 (CRC Press, 2023).

16. Lv, W. et al. VO₂ (B) nanobelts/reduced graphene oxide composites for high-performance flexible all-solid-state supercapacitors. *Sci. Rep.* **9**(1), 10831 (2019).
17. Hou, Z. Q., Wang, Z. Y., Yang, L. X. & Yang, Z. G. Nitrogen-doped reduced graphene oxide intertwined with V₂O₃ nanoflakes as self-supported electrodes for flexible all-solid-state supercapacitors. *RSC Adv.* **7**(41), 25732–25739 (2017).
18. Zheng, J. et al. V₂O₃/C nanocomposites with interface defects for enhanced intercalation pseudocapacitance. *Electrochim. Acta* **318**, 635–643 (2019).
19. Hu, T. et al. Encapsulating V₂O₃ nanorods into carbon core-shell composites with porous structures and large specific surface area for high performance solid-state supercapacitors. *Microporous Mesoporous Mater.* **262**, 199–206 (2018).
20. Zhang, X., Bu, Z., Xu, R., Xie, B. & Li, H. Y. V₂O₃ nanofoam@ activated carbon composites as electrode materials of supercapacitors. *Funct. Mater. Lett.* **10**(06), 1750077 (2017).
21. Nagaraju, D. H., Wang, Q., Beaujuge, P. & Alshareef, H. N. Two-dimensional heterostructures of V₂O₅ and reduced graphene oxide as electrodes for high energy density asymmetric supercapacitors. *J. Mater. Chem. A* **2**(40), 17146–17152 (2014).
22. Liu, Z., Zhang, H., Yang, Q. & Chen, Y. Graphene/V₂O₅ hybrid electrode for an asymmetric supercapacitor with high energy density in an organic electrolyte. *Electrochim. Acta* **287**, 149–157 (2018).
23. Zhong, S. et al. Enhanced fast-charging capability in spinel LiMn₂O₄ via K⁺ ion stabilization for advanced lithium-ion batteries. *ACS Appl. Energy Mater.* **8**(7), 4395–4403 (2025).
24. Capón, C. R., Vilatela, J. J. & Pendashteh, A. High-power and high-energy zinc ion cathodes through embedded CNTs current collectors in vanadium oxide. *Electrochim. Acta* **512**, 145453 (2025).
25. Zhou, M., Gomez, J., Li, B., Jiang, Y. B. & Deng, S. Oil tea shell derived porous carbon with an extremely large specific surface area and modification with MnO₂ for high-performance supercapacitor electrodes. *Appl. Mater. Today* **7**, 47–54 (2017).
26. Malak-Polaczyk, A., Matei-Ghimbeu, C., Vix-Guterl, C. & Frackowiak, E. Carbon/λ-MnO₂ composites for supercapacitor electrodes. *J. Solid State Chem.* **183**(4), 969–974 (2010).
27. Zhang, X., Sun, X., Zhang, H., Zhang, D. & Ma, Y. Development of redox deposition of birnessite-type MnO₂ on activated carbon as high-performance electrode for hybrid supercapacitors. *Mater. Chem. Phys.* **137**(1), 290–296 (2012).
28. Huang, T., Qiu, Z., Wu, D. & Hu, Z. Bamboo-based activated carbon@ MnO₂ nanocomposites for flexible high-performance supercapacitor electrode materials. *Int. J. Electrochem. Sci.* **10**(8), 6312–6323 (2015).
29. Zhang, J. et al. Preparation and electrochemistry of hydrous ruthenium oxide/active carbon electrode materials for supercapacitor. *J. Electrochem. Soc.* **148**(12), A1362 (2001).
30. Fischer, A. E., Pettigrew, K. A., Rolison, D. R., Stroud, R. M. & Long, J. W. Incorporation of homogeneous, nanoscale MnO₂ within ultraporos carbon structures via self-limiting electroless deposition: Implications for electrochemical capacitors. *Nano Lett.* **7**(2), 281–286 (2007).
31. Fu, M. et al. Facile synthesis of V₂O₅/graphene composites as advanced electrode materials in supercapacitors. *J. Alloy. Compd.* **862**, 158006 (2021).
32. Tan, Y., Xi, M., Zhu, Y. & Xu, Z. Nanostructured Mn-doped V₂O₅/carbon belts aggregation spheres composite synthesized via hydrothermal method for supercapacitors. *Diam. Relat. Mater.* **141**, 110667 (2024).
33. Dandekar, M. S., Arabale, G. & Vijayamohan, K. Preparation and characterization of composite electrodes of coconut-shell-based activated carbon and hydrous ruthenium oxide for supercapacitors. *J. Power Sources* **141**(1), 198–203 (2005).
34. Kim, H. & Popov, B. N. Characterization of hydrous ruthenium oxide/carbon nanocomposite supercapacitors prepared by a colloidal method. *J. Power Sources* **104**(1), 52–61 (2002).
35. Yadav, M. S., Sinha, A. K. & Singh, M. N. Electrochemical behaviour of ZnO-AC based nanocomposite electrode for supercapacitor. *Mater. Res. Express* **5**(8), 085503 (2018).

Acknowledgements

One of the authors, Fateh Singh Gill, is thankful to the Chairman of Graphic Era (Deemed to be University), Dehradun, for supporting this research.

Author contributions

Monika Dumka: Conceptualization, Methodology, Investigation (synthesis and characterization), Formal Analysis (electrochemical data), Writing—Original Draft. Sakshi Juyal: Methodology, Investigation (synthesis, antimicrobial assays), Data Curation, Writing—Original Draft. Akansha Rajput: Investigation (electrochemical testing, Raman analysis), Visualization, Writing—Review and Editing. Fateh Singh Gill: Supervision, Project Administration, Funding Acquisition, Resources, Validation. Ankit Sharma: Investigation (TEM/SEM characterization), Formal Analysis (morphological data), Writing—Review and Editing. Vivek John: Resources (electrochemical instrumentation), Validation, Data Interpretation. Vijay Kumar: Supervision (electrochemical studies), Methodology Validation, Writing—Review and Editing. Prumal Asaithambi: Conceptualization, Supervision, Writing—Review and Editing, Project Coordination, Corresponding Author. All authors reviewed and approved the final manuscript.

Declarations

Competing interests

The authors declare no competing interests.

Additional information

Correspondence and requests for materials should be addressed to F.S.G. or P.A.

Reprints and permissions information is available at www.nature.com/reprints.

Publisher's note Springer Nature remains neutral with regard to jurisdictional claims in published maps and institutional affiliations.

Open Access This article is licensed under a Creative Commons Attribution-NonCommercial-NoDerivatives 4.0 International License, which permits any non-commercial use, sharing, distribution and reproduction in any medium or format, as long as you give appropriate credit to the original author(s) and the source, provide a link to the Creative Commons licence, and indicate if you modified the licensed material. You do not have permission under this licence to share adapted material derived from this article or parts of it. The images or other third party material in this article are included in the article's Creative Commons licence, unless indicated otherwise in a credit line to the material. If material is not included in the article's Creative Commons licence and your intended use is not permitted by statutory regulation or exceeds the permitted use, you will need to obtain permission directly from the copyright holder. To view a copy of this licence, visit <http://creativecommons.org/licenses/by-nc-nd/4.0/>.

© The Author(s) 2025